Available online at www.sciencedirect.com
ScienceDirect
Journal of Colloid and Interface Science 313 (2007) 152–159
JOURNAL OF Colloid and Interface Science
www.elsevier.com/locate/jcis

Stable cluster formation in aqueous suspensions of iron oxyhydroxide nanoparticles

Benjamin Gilbert [a,*], Guoping Lu [a], Christopher S. Kim [b]

[a] *Earth Sciences Division, Lawrence Berkeley National Laboratory, Berkeley, CA 94720, USA*
[b] *Department of Physical Sciences, Chapman University, Orange, CA 92866, USA*

Received 27 October 2006; accepted 17 April 2007

Available online 20 April 2007

Abstract

Metal oxide and oxyhydroxide nanoparticles are important components of natural aqueous systems and have application in photocatalysis. Uncoated (oxyhydr)oxide nanoparticles can form charge-stabilized colloids in water, but the precise regimes of dispersion and aggregation have been determined for very few nanomaterials. We studied the colloidal behavior of ~6 nm nanoparticles of iron oxyhydroxide (FeOOH), a common natural nanoscale colloid, and found that these nanoparticles formed stable suspended clusters under a range of aqueous conditions. Light and X-ray scattering methods show that suspended fractal nanoclusters are formed between pH 5 and 6.6 with well-defined maximum diameters that can be varied from 25 nm to approximately 1000 nm. The nanoclusters retain a very high surface area, and persist in suspension for at least 10 weeks in solution. The process is partially reversible because optically transparent suspensions are regained when nanoparticles that aggregated and settled at pH >7 are adjusted to pH 4 without stirring. However, completely redispersed nanoparticles are not obtained even after one month. Because nanocluster formation is controlled predominantly by surface charge, we anticipate that many metal oxide and other inorganic nanoparticles will exhibit equivalent cluster-forming behavior. Our results indicate that natural nanoparticles could form stable nanoclusters in groundwater that are likely to be highly mobile, with implications for the long-range transport of surface sorbed contaminants.
© 2007 Elsevier Inc. All rights reserved.

Keywords: Nanoparticles; Clusters; Aggregation; Colloid transport; Small-angle X-ray scattering; Dynamic light scattering; Photon correlation spectroscopy

1. Introduction

Colloids are of widespread importance in numerous areas of science, medicine, and engineering [1,2], and of enduring theoretical interest due to the rich behavior that can emerge from apparently simple systems. The conceptual basis of the colloidal behavior of particle suspensions is well established for micron and submicron particles, although quantitative discrepancies persist [3], and surprising behavior, such as colloid jamming [4], has been recently observed. Quantitative experimental tests of the regimes of colloid stability and of aggregation behavior have clarified the validity and limitations of the classical descriptions of colloids. However, nanoparticle suspensions represent an increasingly common colloid because nanomaterials can be produced that possess modified mechanical, optical and electronic properties relative to the bulk. While considerable effort has been directed at making nanoparticles with narrow size distributions that are dispersible in water or in organic media, there have been very few studies of the colloidal behavior of such systems. Moreover, there is now considerable evidence that mineral nanoparticles are common components of natural aqueous systems. Numerous natural inorganic and biologically mediated processes produce mineral nanoparticles such as metal sulfides and metal oxides that can be exceedingly small (<10 nm) [5,6]. Nanoscale iron (oxy)hydroxide phases are among the most common natural mineral nanoparticles [7,8], formed by precipitation from solution following oxidation of aqueous ferrous iron.

Natural nanoparticles exhibit size dependent trends in structure and reactivity that are analogous to those found in synthetic materials [9]. Because the chemistry of these materials involves surface processes, the dispersion behavior of nanoparticles is an important aspect of their effective reactivity in both environ-

* Corresponding author. Fax: +1 510 486 5686.
E-mail address: bgilbert@lbl.gov (B. Gilbert).

0021-9797/$ – see front matter © 2007 Elsevier Inc. All rights reserved.
doi:10.1016/j.jcis.2007.04.038

mental and technological settings. Moreover, aggregation is a major factor determining the transport of environmental particles [10], which can move material between redox zones and facilitate or inhibit contaminant transport. Although environmental colloidal particles frequently aggregate in circumneutral water, studies have indicated that certain nanoscale colloids have the ability to travel unexpectedly large distances in the environment [11–13]. Despite numerous observations that nanoscale minerals represent an important fraction of environmental colloids [5–9,11], the fundamental aggregation and transport properties of nanoparticles have not yet been established. We addressed these topics with a study of the colloidal properties of iron oxyhydroxide (α-FeOOH) nanoparticles with diameters of approximately 6 nm.

2. Materials and methods

2.1. Nanoparticle synthesis and characterization

The synthesis method chosen for this work has been used for several independent studies of FeOOH nanoparticle adsorption properties and reactivity [14–16]. Dispersed iron oxyhydroxide nanoparticles were synthesized as follows. 10 mL of 2.4 M $NaCO_3$ was added dropwise to 25 mL of 0.2 M $Fe(III)(NO_3)_3$ during rapid stirring to reach pH 2. Rapid hydrolysis and precipitation was induced by microwave heating at approximately 35 s intervals until the solution had just reached a full boil. Further reaction and particle growth was immediately quenched by plunging the flask into iced water. This procedure was repeated an additional 3 times. The resulting suspension was dialyzed in 1000 MWCO membranes (SpectrumLabs) for at least 3 days against a solution of HNO_3 in ultrapure water at pH 4, replacing the dialysis bath solution regularly. All water used in these experiments was purified to greater than 18 MΩ (Elga UHQ 2) and filtered through 0.1 μm pore membranes. The synthesis method produced a suspension of FeOOH nanoparticles at a concentration of 6.5 g/L. The surface area was determined by the BET method to be 306 ± 1 m^2/g. The crystal phase was investigated by X-ray diffraction, and found to be consistent with a nanoscale and/or highly disordered goethite (α-FeOOH) phase (supplementary Fig. S1). The particle size was determined to be 6 ± 1 nm by high-resolution transmission electron microscopy (Fig. S2).

2.2. Potentiometric titrations

We performed potentiometric (acid–base) titrations of solutions of FeOOH nanoparticles at three ionic strengths to determine the point of zero net surface charge (pH_{znsc}) and the variation of surface charge as a function of pH. We followed standard procedures [17,18], with the exception that CO_2 was not excluded from the nanoparticle suspension prior to the titration. (The consequences of the presence of CO_2 are shown by an aqueous speciation calculation given in Fig. S3.) Specifically, 39 mL of a dialyzed nanoparticle suspension at pH 4 and FeOOH concentration of 6.5 g/L was titrated in a Mettler–Toledo DL50 autotitrator against a freshly prepared solution of 0.0059 M NaOH in ultra pure water. The solution ionic strength was determined by $NaNO_3$ addition, and titrations were performed at 10^{-3}, 10^{-2} and 10^{-1} M $NaNO_3$. The pH was recorded with a Mettler–Toledo combination glass pH electrode that was calibrated with buffers at pH 4, 7 and 10 between each measurement. Each titration took approximately 20 min with a step size of approximately 8 mV. A measurement was recorded once the drift was less than 0.1 mV/s. Separately, background titrations of pH 4 HNO_3 solutions at the same $NaNO_3$ concentrations were performed. The surface charge density was calculated from the titration results by subtracting the blank titration curve from the data and converting the adsorbed proton quantities into charge density using the surface area determined by BET analysis.

2.3. Small-angle X-ray scattering analysis

We acquired small-angle X-ray scattering data from solutions containing FeOOH nanoparticles as a function of pH from pH 4–10 at a temperature range of 21–23 °C. In order to avoid dilution when the solution conditions were altered, the pH was varied by dialyzing nanoparticle solutions against 3 L baths at successively higher pH. The SAXS data were acquired from Stanford Synchrotron Radiation Laboratory (SSRL) beamline 1–4 at 8.333 keV using a configuration that maximized the accessible q-range, attaining almost two orders of magnitude in q. Approximately 0.4 mL of solution was drawn into a SAXS liquid cell with kapton windows and a 1 mm X-ray path length. 2D scattering patterns were collected on a CCD based area detector (Roper) from the sample mounted in one of two positions for acquisition times of 4 min (high-q position) or 8 min (low-q position). The CCD data was binned into 1D intensity data on a calibrated q-axis using macros written in the Image-Pro Plus software by John Pople.

All SAXS data were first processed by subtracting a CCD background (obtained from an X-ray free exposure). Subsequent subtraction of the blank solvent scattering pattern resulted in SAXS data associated with the nanoparticles alone. The measured intensity of the SAXS data from the two positions differed by a geometrical scaling factor that was fitted from the overlapping portion of the data. Data reduction and further analysis was performed with routines written in the Igor-Pro software (Wavemetrics). The mean diameter and fractal dimension of the nanoparticle clusters were estimated by fitting an analytical expression for the SAXS scattering intensity from fractal aggregates to the treated data [20,21]. The SAXS structure factor for fractal aggregates of spherical particles of radius a and fractal dimension, d_f, is calculated from:

$$S(q) = 1 + \frac{1}{(qa)^{d_f}} \frac{2a\Gamma(a-1)}{(a-1)} \sin\left[(a-1)\tan^{-1}(q\xi)\right] \times \left(1 + \frac{1}{(q\xi)^2}\right), \quad (1)$$

where $\Gamma(a-1)$ is the gamma function and ξ is the large-size cut-off in the aggregate density distribution function. A finite size distribution of particle sizes (obtained from a fit to SAXS

data from low pH, dispersed dilute nanoparticles) is incorporated numerically.

2.4. Dynamic light scattering analysis

We performed dynamic light scattering (DLS) measurements of the aqueous diffusion coefficient of dispersed nanoparticles and nanoparticle clusters as a function of solution pH at a temperature that was maintained at 25 °C. DLS analysis was performed with a PD-Expert Workstation (Precision Detectors, Bellingham, MA) fitted with a quartz flow-through cell. Laser light ($\lambda = 685$ nm) scattered through 135° was sent via glass fiber to an optical correlator.

Approximately 0.4 mL of sample was used per measurement, and ~2 mL of rinsing solution (pH 4 HNO_3) was injected between measurements. Blank acquisitions were acquired between samples to ensure no cross-contamination. The number of repeats for a single acquisition was chosen to ensure that the noise on the data was less than 0.1% in the correlation functions, and typically 256 2 s exposures were averaged. A dust cut-off filter was built into the data acquisition software. The determination of the distribution of aggregate sizes was performed using proprietary Precision Detectors software (PrecisionDeconvolve) that employs a regularization algorithm [22] to seek a smooth, non-negative size distribution function that provides the best fit to the data. It has been shown that low noise DLS data analyzed with this method can resolve multimodal distributions provided the diffusion coefficients differ by greater than a factor of ~2.5.

2.5. Calculation of DLVO interaction energies

We selected analytical expressions for the electrostatic and van der Waals potentials between spherical particles of radius a, separated by distance, h, that were valid for $h > a$ and for large values of the surface potential (i.e., greater than 25 mV). The DLVO interaction is the sum of two contributions:

(1) Screened Coulomb interactions. The electrostatic interaction energy, U_C, between two identical spheres of radius a, and separation h, is given by [2]:

$$U_C = 64\pi\varepsilon\varepsilon_0 \frac{a}{2}\left(\frac{kT}{e}\right)^2 \gamma^2 e^{-\kappa h}, \tag{2}$$

where ε is the relative permittivity of the medium (for water, $\varepsilon \approx 78$), ε_0 is the permittivity of free space, k is Boltzmann's constant, and T is the temperature in K, and e the charge of the electron. The reciprocal Debye length is:

$$\kappa = \sum_i \sqrt{\frac{8\pi c_i e^2 z_i^2}{\varepsilon\varepsilon_0 kT}}, \tag{3}$$

where $z_i e$ is the charge on an aqueous ion of valence z_i, and c_i is the ion concentration in m^{-3}.

The term, γ, is related to the surface potential, ψ, by $\gamma = \tanh(\frac{(e\psi)}{(4kT)})$. The surface potential is calculated from the measured surface charge density, σ, using the Grahame equation:

$$\psi = \frac{kT}{2ze}\sinh^{-1}\left(\frac{\sigma}{\sqrt{8kTc\varepsilon\varepsilon_0}}\right). \tag{4}$$

(2) Van der Waals interactions. The non-retarded van der Waals interaction between identical spheres of radius a, and separation h, was derived by Hamaker [23] as:

$$U_{vdW} = -\frac{A}{6}\left[\frac{2a^2}{h^2+4ah} + \frac{2a^2}{h^2+4ah+4a^2} + \ln\left(\frac{h^2+4ah}{h^2+4ah+4a^2}\right)\right], \tag{5}$$

where A is the Hamaker constant. Because no determination of this constant has been published for goethite, we selected a value for the Hamaker constant that is in the middle of the values that have been proposed for the hematite–water–hematite system [18,24–26]:

$$A_{\text{hematite}} = 4 \times 10^{-20}\ \text{J}.$$

3. Results

3.1. Potentiometric titration

The results of the potentiometric titrations are plotted in Fig. 1. The common intersection point for the 3 titration curves was identified with the pH of zero net surface charge: pH_{znsc} 8.65 ± 0.04. This value, and the quantitative surface charge density curves are in good agreement with prior studies of the surface charge density of goethite equilibrated with atmospheric CO_2 [19].

3.2. Observation of nanocluster formation

3.2.1. Small-angle X-ray scattering

We used in situ small-angle X-ray scattering (SAXS) to investigate the colloid stability of the nanoparticle suspensions as a function of pH and ionic strength. The SAXS data from samples below pH 5 are typical for a completely dispersed colloid suspension (Fig. 2a). Above pH ~6.6, the SAXS profiles

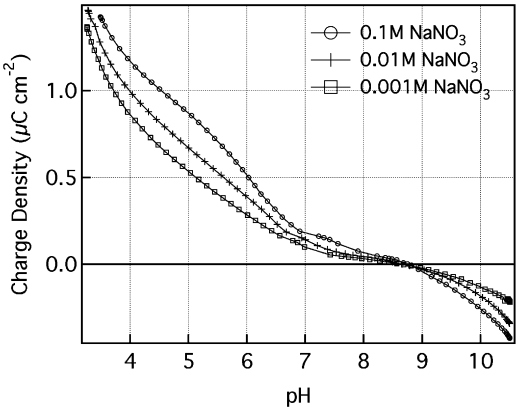

Fig. 1. The surface charge density vs. pH of iron oxyhydroxide nanoparticles as a function of solution ionic strength, obtained from potentiometric titration measurements.

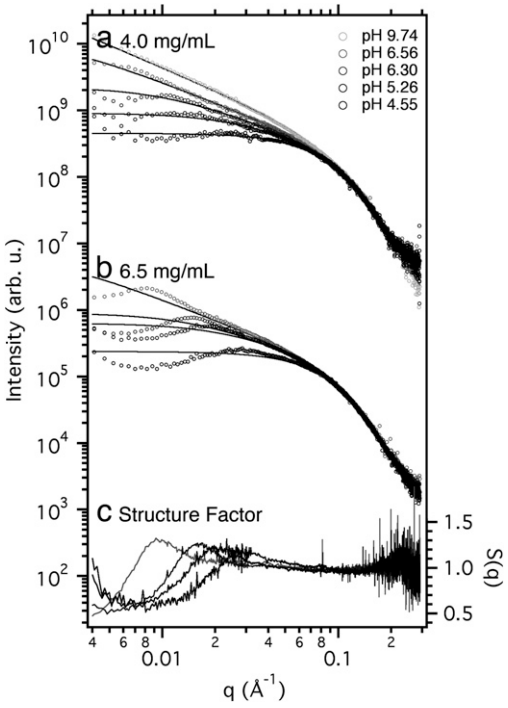

Fig. 2. Small-angle X-ray scattering (SAXS) evidence for cluster formation. (a) and (b) SAXS data (○) as a function of pH from suspensions of iron oxyhydroxide nanoparticles at a concentration of 4.0 mg/mL (volume fraction, $\phi \approx 0.001$) (a), and a concentration of 6.5 mg/mL ($\phi \approx 0.0015$) (b). (c) The structure factor, $S(q)$, obtained by dividing the high concentration data by the fits to the lower concentration data. These fits are shown by the smooth grey lines in the top two patterns. All data were acquired in 10^{-3} M $NaNO_3$.

are typical for large-scale fractal aggregates, indicating that extensive aggregation has occurred. However, between pH 5–6.6 we observed the formation of nanoclusters that were stable against further aggregation. The SAXS profiles from samples in this regime are characteristic of nanoscale fractal aggregates with increasing dimensions. Analogous intensity profiles have been recorded by static light scattering during continuous aggregation of micron-sized silica spheres [26]. In the present system, however, SAXS patterns exhibit only very slight evolution even after 10 weeks at room temperature (see below), indicating that aggregation has been arrested. After more than four months, these suspensions remain visually transparent, indicating that macroscopic aggregation has still not yet occurred.

The cause of the arrested aggregation is illuminated by SAXS data acquired at higher particle concentration (Fig. 2b). These SAXS patterns exhibit additional structure that is typical for a suspension of objects in solution experiencing mutually repulsive electrostatic interactions [28]. Under such circumstances, the SAXS intensity may be factored into a form factor, $P(q)$, associated with individual nanoparticles or nanoclusters, and a structure factor, $S(q)$, caused by their mutual repulsion. We obtained $S(q)$ from the SAXS intensity data and display this in Fig. 2c. From the form of $S(q)$ we conclude that the nanoclusters experience a repulsive electrostatic barrier to further aggregation [28], with both the size and interior structure of the nanoclusters appearing to be strongly affected by the long-range Coulombic interactions. Fits to the SAXS patterns for dilute nanoclusters gave fractal dimensions (d_f) in the range 1.1–1.2, significantly lower than expected for either diffusion limited ($d_f \approx 1.8$) or reaction limited ($d_f \approx 2.1$) particle aggregation mechanisms [20]. This value is very close to unity, the minimum value that is geometrically possible for a single contiguous object in three dimensions.

We carefully checked for background subtraction errors that might have caused erroneous slopes in the SAXS data, and excluded this possibility. Similarly low fractal dimension values were acquired repeatably for this system over three SAXS experiments. Data acquired at the same beamline on a different system (precipitates of nanocrystalline FeS) gave fractal dimension values close to $d_f \approx 2.1$, ruling out a systematic error in sample acquisition or analysis.

It is reasonable to conclude that the nanoclusters possess very open structures in order to minimize their total electrostatic energy. However, theoretical expressions for the SAXS profiles from such small clusters are presently very inaccurate, and thus it is not possible to estimate the error on the fitted values. Analytical expressions are most reliable when the aggregate size is large relative to the primary particle size [30]. Despite theoretical treatments [20,31] and simulation [32], there are no universally accepted treatments of the low-q and high-q regions. These regions correspond, respectively, to the large-scale maximum extent of the fractal aggregate, and small-scale structure at the length scale of the primary particles. The structure of real aggregates does not satisfy ideal fractal geometry at these limits. This problem is particularly acute for the data in Fig. 2, for which the cluster sizes are so small that the linear region in the log–log SAXS intensity plot that is characteristic of extended fractal aggregates is barely developed.

3.2.2. *Dynamic light scattering*

Because the range of cluster dimensions accessible by SAXS is limited, we repeated the experiment, analyzing the nanocluster dimensions with dynamic light scattering (DLS) [26,27,29]. In these studies, a finer step size in pH was obtained using an autotitrator to make injections of 0.001 M NaOH to a stirred suspension of nanoparticles initially at pH 4. The DLS measurements were analyzed to obtain the cluster size distributions, in particular the mean hydrodynamic radius, R_H, as a function of pH. Examples of DLS raw data are given in Fig. S5, and the results of these experiments are summarized in Fig. 3. In agreement with the SAXS measurements, we observe that raising the pH above pH 5 leads to the initiation of aggregation, but for pH <6.6 this process is arrested at submicron cluster sizes. DLS measurements are highly sensitive to the presence of larger scattering objects, and no weighting is applied that would suppress this. Thus, the DLS data show that, when submicron nanoclusters are formed, there are no aggregates in solution that are larger than the sizes indicated in Fig. 3. This conclusion is consistent with visual inspection of the suspensions, which remain optically clear with no particulates or sediment in this pH range (see digital photograph in Fig. S6). In the absence of hydrodynamic shear stress, the colloidal system frequently formed

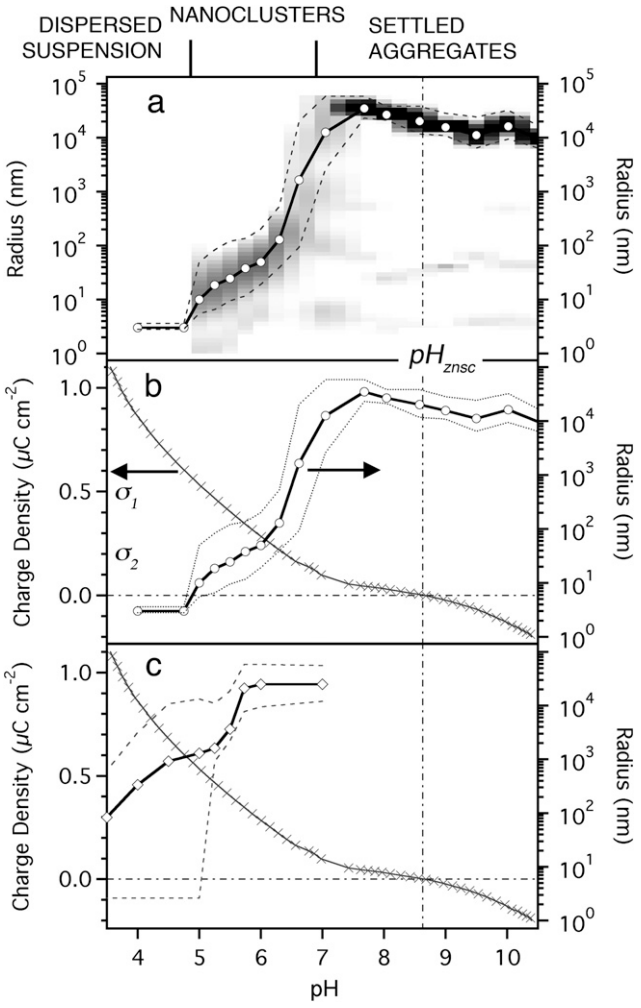

Fig. 3. Dynamic light scattering (DLS) observations of pH-driven cluster formation and disaggregation at room temperature and in 10^{-3} M $NaNO_3$. (a) Compilation of DLS size histograms observed as the pH of an aqueous suspension of FeOOH nanoparticles is raised from pH 4 to 10.5. The individual histograms are converted into a two-dimensional image plot. (○) Show the DLS mean cluster radii; (- - -) illustrate the distribution of cluster radii by enclosing 95% of the size histogram. (b) Aggregation: the pH dependence of cluster size distributions (right axis), obtained from the procedure depicted in (a), plotted against the nanoparticle surface charge density (left axis), obtained from potentiometric titrations (cf. Fig. 1). The pH was increased by the addition of NaOH base, and the DLS measurements acquired within several hours. σ_1 and σ_2 are estimates of the threshold values of surface charge density at which cluster formation and macroscopic aggregation occur as pH is raised—i.e., they enclose the regime of nanocluster formation. (c) Disaggregation: The pH dependence of the cluster size distributions during the disaggregation process. The pH was decreased by the addition of HNO_3 acid, and the DLS measurements acquired after three weeks.

a gel at pH ∼7. Above this pH, large aggregates are formed that settle under the influence of gravity.

3.3. The long-term stability of FeOOH nanoparticle clusters

Fig. 4 shows the change in the SAXS data following 10 weeks aging at room temperature for nanocluster samples stored at pH 4.8–6.3. For pH <6, there is evidence of a small increase in nanocluster size that is seen from the shift in the low-q peak to lower q-values. (The positions of intensity features in

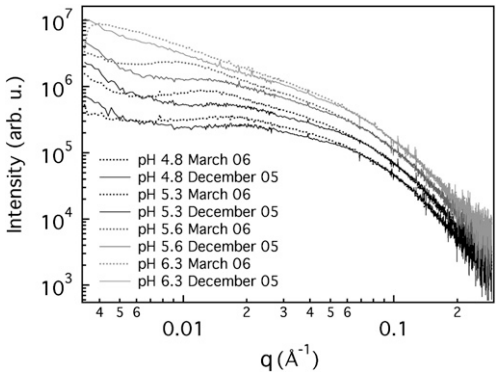

Fig. 4. Small-angle X-ray scattering (SAXS) data acquired from the same suspensions of FeOOH nanoparticles at different dates. Following a 10-week aging period at room temperature, the nanoclusters exhibit very slight growth.

q-space SAXS data are inversely related to real-space distances in the sample.) There is also an increase in the gradient of the linear regions that is likely correlated with increasing cluster density and fractal dimension. Simple fits assuming ideal fractal aggregates indicate that any size increases are of the order of a few percent in cluster diameter, and less than 0.1 unit in fractal dimension. It is presently impossible to perform very accurate analyses of cluster size changes due to the lack of an accurate expression for the scattering from such small nanoparticle clusters. Although we have not yet had an opportunity to further investigate the stability of these clusters with SAXS at longer times, after 4 months there is no visible aggregation in these samples. DLS observations of nanocluster suspensions confirm the SAXS observations for pH <6. Above this pH, further slow aggregation is observed (Fig. S7).

3.4. Tests of reversibility

We tested the reversibility of the nanoparticle aggregation by dialyzing a suspension of nanoparticles to pH 9.6 and then incrementally lowering the pH with 0.01 M HNO_3 additions. The samples were equilibrated for 3 weeks with no agitation, and then analyzed with DLS. Below pH ∼5.7, a small portion of the material is resuspended into the liquid phase, while most remains as a sediment. Visual observations (Fig. S9) clearly show that the resuspended fraction increases as the pH is lowered. Below pH ∼4, an optically clear solution is eventually obtained, although a DLS analysis shows that a dispersion of individual nanoparticles is never regained, even at pH 3.5. Instead, the size distribution of the resulting nanoclusters is considerably greater than is found in a suspension that has not been completely aggregated. A summary of DLS observations of the disaggregation process is included in Fig. 3c and more details are given in Figs. S8–S10.

4. Discussion

4.1. An example of nanoparticle cluster formation

It is well established that the conditions under which micron scale colloidal particles aggregate can be understood in terms

of competing attractive and repulsive forces between pairs of particles, as described by the classical Derjaguin–Landau–Verwey–Overbeek (DLVO) theory of colloidal behavior. Within DLVO theory, particles possessing like charge may be kinetically stabilized against aggregation by their mutual repulsion. For solution conditions in which the barrier against particle–particle aggregation can be overcome by available thermal energy (k_BT), complete aggregation occurs at a rate controlled by the interparticle potentials [18]. In the present system, however, the interparticle interactions control not only the rate of aggregation but also the ultimate aggregate size, leading to the formation of stable nanoclusters.

Cluster formation is an important recent concept in colloid science. Theoretical models have described cluster formation in several classes of colloids:

(i) Colloids possessing "sticky hard sphere" characteristics exert negligible long-range repulsive interactions but interact at close range via an adhesion parameter, $\varepsilon \sim k_BT$. It is likely that several experimental observations of cluster formation in micron-sized spheres are of this type [33–36]. Optical imaging has shown that clusters and monomers coexist for a range of ε and volume fraction [34–36].

(ii) Colloids that interact only via short-range repulsive interactions can, in the presence of solvent–colloid hydrodynamic interactions, reach a dynamic equilibrium of aggregation–fragmentation with a population of clusters exhibiting an exponential number distribution [37].

(iii) For colloids possessing significant long-range repulsive interactions, it is intuitive that this interaction may limit the size of aggregates, as has been predicted by several investigators [38,39]. The combination of short-range attractive and long-range repulsive interactions can arrest aggregation and cause the development of a monomodal distribution of cluster sizes [39].

There are presently no clear experimental criteria for distinguishing the driving forces for cluster formation. For nanoscale colloids, it is presently unclear how accurately in situ scattering techniques can determine cluster size distributions. For FeOOH suspensions, there is no evidence that nanoclusters coexist with free nanoparticles, but the latter are likely difficult to detect by SAXS or DLS in the presence of larger clusters. Nevertheless, many features of cluster formation in FeOOH nanoparticles, as well as elementary considerations, lead to the conclusion that cluster stabilization is controlled by Coulombic repulsive interactions, particularly because cluster dimensions are tunable with pH, varying over 2 orders of magnitude. Moreover, the nanocluster size does not exhibit a detectable dependence on nanoparticle concentration in the concentration ranges investigated in the present study. A calculation of the interaction forces confirms that this conclusion is feasible, and emphasizes the role of next-nearest-neighbor interactions in cluster stabilization.

4.2. The role of next-nearest-neighbor interactions

We investigated the origin of the nanocluster formation by comparing the ideal interparticle potential curves for the present system with those for a hypothetical suspension of larger (30 nm), but otherwise identical FeOOH nanoparticles. These curves, given in Fig. 5, show that for 6 nm diameter nanoparticles, significant repulsive Coulombic forces are felt by two particles that are separated by one particle diameter. These next-nearest-neighbor (NNN) interactions are important energetic contributions that reduce aggregate stability. By contrast, for particles that are only 5 times larger, NNN interactions are negligible, and the aggregation behavior can be understood by considering two-body interactions alone. Our simple calculation suggests that the destabilizing NNN interactions are less than the thermal energy available at 298 K. (A recent theoretical development providing more accurate treatment of dispersion forces indicates that our approach overestimates the attractive interaction between nanoparticles [40].) Nevertheless, these repulsive interactions will act cumulatively to inhibit the formation of aggregates that are larger than a critical size. Because electrostatic interactions are a dominant contribution, the cluster size can thus be controlled by pH.

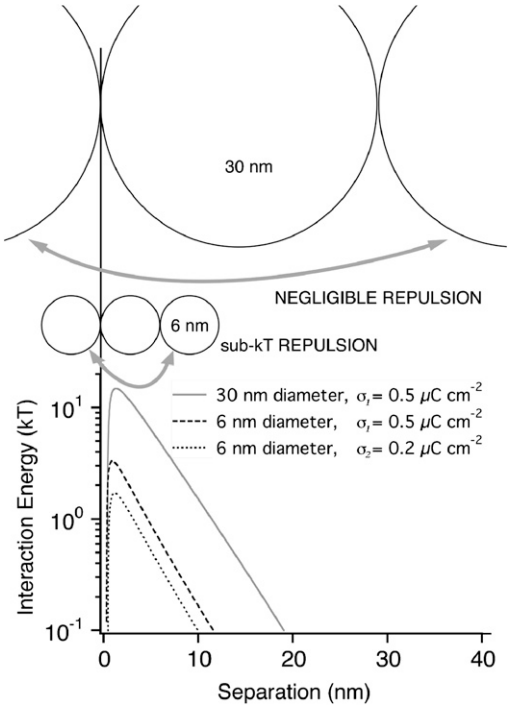

Fig. 5. The effect of particle size on colloidal particle interaction energies. The DLVO interaction energy, expressed in terms of the thermal energy, kT, available at 298 K is calculated vs. interparticle separation for 6 and 30 nm diameter iron oxide nanoparticles in a monovalent symmetrical electrolyte at 10^{-3} M. For the smaller particle size, the interaction energies are plotted for the surface charge densities, σ_1 and σ_2, that are determined from Fig. 3 to delineate the region of nanocluster formation. The maximum in the potential energy curves presents an activation barrier against aggregation that increases with the particle dimension and the surface charge. Repulsive next-nearest-neighbor interactions that approach kT are present between the nanoscale particles, but completely negligible for particles only 5 times larger.

4.3. Significance of incomplete disaggregation

Although settled macroscopic aggregates can be partially disaggregated and resuspended as smaller nanoclusters at room temperature, completely dispersed nanoparticles are never regained. The size distribution of the resulting nanoclusters is considerably greater than is found in a suspension that has not been completely aggregated. These observations indicate that short-range chemical interactions that are not included in classical DLVO theory are important between aggregated nanoscale particles [26]. Indeed, prior work has shown that chemical interactions at the interface between aggregated nanoparticles can cause reversible structural changes [41] and mediate electronic superexchange interactions between the magnetic structures of neighboring nanoparticles [42]. Furthermore, the aggregation of nanoparticles is the first step in growth by oriented attachment (OA). In the OA process, growth proceeds via the epitaxial [43,44] or partially-misaligned [45] addition of primary particles. Strong, crystal-face specific chemical interactions must be responsible for the alignment of nanoparticles during this growth process. We infer that a fraction of aggregated nanoparticles are crystallographically aligned and attached via strong chemical interactions, preventing subsequent surface charge-driven disaggregation. Thus, the large size distributions observed in the disaggregation experiments are likely a signature of the early stages of oriented aggregation.

5. Conclusions

5.1. Cluster formation in nanoparticle suspensions

Our observations are relevant to many systems because we expect that nanoparticles of any material for which proton adsorption determines surface charge will form stable nanoclusters over a wide range of aqueous conditions. Fig. 3 clearly shows that there are threshold values of surface charge density at which (i) cluster formation and (ii) settling occur as pH is increased. We anticipate that these onsets should be predictable from surface charge vs pH curves and the Hamaker constant. Surface organic molecules are frequently present on nanoparticle surfaces in natural and technological settings. Although such molecules may possess functional groups with different acid-base characteristics than the inorganic surface, their presence is expected only to shift the regime in which nanocluster formation occurs, not produce qualitatively different behavior. Consequently, our observations indicate the need to tailor solvent conditions to ensure that the effects of long-range repulsive interactions do not limit the maximum colloidal crystal sizes attainable by the self-assembly of surfactant-coated nanoparticles [46]. It is known that the hydrodynamic properties of aggregates and hence nanoclusters are considerably different from the dispersed particles [20]. Hence, nanocluster formation would deleteriously affect the thermal transport properties of nanofluids [47] and membrane filtration processes involving nanoparticles [10].

5.2. Implications for the transport of environmental nanoparticles

From the considerations described above, it is likely that many naturally occurring silicate and aluminum (oxy)hydroxide nanoparticles (pH_{znsc} 2.0–3.5) may form nanoclusters at circumneutral pH. The mobility of natural or synthetic nanoparticles in the natural environment will strongly depend on whether the nanoparticles remain completely dispersed, aggregate and settle, or form mobile nanoclusters. The transport of contaminants in the environment is often determined by the colloidal size fraction [48–50]. For example, FeOOH and AlOOH nanoparticles are formed in acid mine drainage and can exhibit high affinities for dissolved contaminant ions [51,52]. In addition, uranium-containing nanoparticles may be formed by inorganic and biological processes [53,54]. Colloid filtration theory is known to underestimate the distances traveled by environmental colloids [55]. However, nanoparticle transport may be substantially enhanced by nanocluster formation because simulations indicate that the mobility of nanoparticles in groundwater would be enhanced if they cluster to form micron-scale aggregates (Ref. [2] and Fig. S11). Therefore, experimental studies of nanoparticle transport in porous media [56] and models of colloid-facilitated contaminant transport [57] should consider that the water-dispersible colloidal fraction may contain environmentally significant concentrations of nanoparticle clusters.

Acknowledgments

We thank Young-Shin Jun, Tim Kneafsey, Carl Steefel and Li Yang. SAXS data were acquired on beamline 1–4 at the Stanford Synchrotron Radiation Lab (SSRL), and we thank John Pople, Ellie Fazli and Samuil Belopolskiy. The U.S. Department of Energy, Office of Basic Energy Sciences supports use of the SSRL (Contract No. DE-AC03-76SF00515). Financial support for this work came from the Director, Office of Science, Office of Basic Energy Sciences, of the U.S. Department of Energy under Contract No. DE-AC02-05CH11231 and from Lawrence Berkeley National Lab.

Supplementary information

The online version of this article contains additional supplementary information.

Please visit DOI: 10.1016/j.jcis.2007.04.038.

References

[1] J.N. Israelachvili, Intermolecular and Surface Forces: With Applications to Colloidal and Biological Systems, Academic Press, New York, 1992.
[2] M. Elimelech, J. Gregory, X. Jia, R.A. Williams, Particle Deposition and Aggregation: Measurement, Modelling and Simulation, Butterworths–Heinemann, Wobrun, MA, 1995.
[3] S.H. Behrens, M. Borkovec, P. Schurtenberger, Langmuir 14 (1998) 1951–1954.
[4] A.I. Campbell, V.J. Anderson, J.S. van Duijneveldt, P. Bartlett, Phys. Rev. Lett. 94 (2005) 208301.
[5] M. Labrenz, et al., Science 290 (2000) 1744.

[6] M. Villalobos, B. Toner, J. Bargar, G. Sposito, Geochim. Cosmochim. Acta 67 (2003) 2649.
[7] C. van der Zee, D.R. Roberts, D.G. Rancourt, C.P. Slomp, Geology 31 (2003) 993.
[8] R.L. Penn, C. Zhu, H. Xu, D.R. Veblen, Geology 29 (2001) 843.
[9] B. Gilbert, J.F. Banfield, Rev. Mineral. Geochem. 59 (2005) 109.
[10] T.D. Waite, A.I. Schafer, A.G. Fane, A. Heuer, J. Colloid Interface Sci. 212 (1991) 264.
[11] A.B. Kersting, D.W. Efurd, D.L. Finnegan, D.J. Rokop, D.K. Smith, J.L. Thompson, Nature 397 (1999) 56.
[12] P. Vilks, L.H. Frost, D.B. Bachinski, J. Contam. Hydrol. 26 (1997) 203.
[13] A.P. Novikov, S.N. Kalmykov, S. Utsunomiya, R.C. Ewing, F. Horreard, A. Merkulov, S.B. Clark, V.V. Tkachev, B.F. Myasoedov, Science 314 (2006) 638.
[14] Y. Guyodo, A. Mostrom, R.L. Penn, S.K. Banerjee, Geophys. Res. Lett. 30 (2003) 1512.
[15] J. Anschultz, R.L. Penn, Geochem. Trans. 6 (2005) 60.
[16] G.A. Waychunas, C.S. Kim, J.F. Banfield, J. Nanopart. Res. 7 (2005) 409.
[17] D.A. Dzombak, F.M.M. Morel, Surface Complexation Modeling. Hydrous Ferric Oxide, Wiley–Interscience, New York, 1990.
[18] M. Schudel, S.H. Behrens, H. Holthoff, R. Kretzschmar, M. Borkovec, J. Colloid Interface Sci. 196 (1997) 241.
[19] T.D. Evans, J.R. Leal, P.W. Arnold, J. Electroanal. Chem. 105 (1979) 161.
[20] G.C. Bushell, Y.D. Yan, D. Woodfield, J. Raper, R. Amal, Adv. Colloid Interface Sci. 95 (2002) 1.
[21] H.S. Chen, J. Teixeira, Phys. Rev. Lett. 57 (1986) 2583.
[22] S.W. Provencher, Comput. Phys. Commun. 27 (1982) 213.
[23] H.C. Hamaker, Physica 4 (1937) 1058.
[24] E. Matijevic, R.J. Kuo, H.J. Kolny, J. Colloid Interface Sci. 80 (1981) 94.
[25] N.H.G. Penners, L.K. Koopal, Colloids Surf. 19 (1986) 337.
[26] L. Liang, J.J. Morgan, Aquat. Sci. 52 (1990) 32.
[27] M. Hermawan, G. Bushell, G. Bickert, R. Amal, Int. J Miner. Process. 73 (2004) 65.
[28] D. Qiu, C.A. Driess, T. Cosgrove, Langmuir 21 (2005) 9964.
[29] S. Romer, C. Urban, V. Lobaskin, F. Scheffold, A. Stradner, J. Kohlbrecher, P. Schurtenberger, J. Appl. Crystallogr. 36 (2003) 1.
[30] T. Nicolai, D. Durand, J.-C. Gimel, Phys. Rev. B 50 (1994) 16357.
[31] M.Y. Yin, R. Klein, H.M. Lindsay, D.A. Weitz, R.C. Ball, P. Meakin, J. Colloid Interface Sci. 137 (1990) 263.
[32] M. Lattuada, H. Wu, M. Morbidelli, J. Colloid Interface Sci. 268 (2003) 106.
[33] K. Kratz, T. Hellweg, W. Eimer, Colloids Surf. A 170 (2000) 137.
[34] A. Stradner, H. Sedgwick, F. Cardinaux, W.C.K. Poon, S.U. Egelhaaf, P. Schurtenberger, Nature 432 (2004) 492.
[35] H. Sedgwick, S.U. Egelhaaf, W.C.K. Poon, J. Phys. Condens. Matter 16 (2004) S4913.
[36] P.N. Segrè, V. Prasad, A.B. Schofield, D.A. Weitz, Phys. Rev. Lett. 86 (2001) 6042.
[37] S. Bastea, Phys. Rev. Lett. 96 (2006) 028305.
[38] J. Groenewold, W.K. Kegel, J. Phys. Chem. B 105 (2001) 11702.
[39] F. Sciortino, S. Mossa, E. Zaccarelli, P. Tartaglia, Phys. Rev. Lett. 93 (2004) 055701.
[40] H.Y. Kim, J.O. Sofo, D. Velegol, M.W. Cole, A.A. Lucas, J. Chem. Phys. 124 (2006) 074504.
[41] F. Huang, B. Gilbert, H. Zhang, J.F. Banfield, Phys. Rev. Lett. 92 (2004) 155501.
[42] C. Frandsen, S. Mørup, Phys. Rev. Lett. 94 (2005) 027202.
[43] R.L. Penn, J.F. Banfield, Geochim. Cosmochim. Acta 63 (1999) 1549.
[44] K.-S. Cho, D.V. Talapin, W. Gaschler, J. Am. Chem. Soc. 127 (2005) 7140–7147.
[45] J.F. Banfield, S.A. Welch, H. Zhang, T.T. Ebert, R.L. Penn, Science 289 (2000) 751–754.
[46] E.V. Shevchenko, D.V. Talapin, N.A. Kotov, S. O'Brien, C.B. Murray, Nature 439 (2006) 55.
[47] R. Prasher, P. Bhattacharya, P.E. Phelan, Phys. Rev. Lett. 94 (2005) 025901.
[48] R. Kretzschmar, T. Schäfer, Elements 1 (2005) 205.
[49] R. Kretzschmar, M. Borkovec, D. Grolimund, M. Elimelech, Adv. Agronomy 66 (1999) 121.
[50] D. Grolimund, M. Borkovec, K. Barmettler, H. Sticher, Environ. Sci. Technol. 30 (10) (1996) 3118.
[51] G. Furrer, B.L. Phillips, K.U. Ulrich, R. Pöthig, W.H. Casey, Science 297 (2002) 2245.
[52] B.M. Chapman, D.R. Jones, R.F. Jung, Geochim. Cosmochim. Acta 47 (1983) 1957.
[53] Y. Suzuki, S.D. Kelly, K.M. Kemner, J.F. Banfield, Nature 419 (2002) 132.
[54] J.M. Wan, T.K. Tokunaga, E. Saiz, J.T. Larsen, Z.P. Zheng, R.A. Couture, Environ. Sci. Technol. 38 (2004) 6066.
[55] L.M. McDowell-Boyer, J.R. Hunt, N. Sitar, Water Resour. Res. 22 (1986) 1901.
[56] H.F. Lacoanet, J.V. Bottero, M.R. Weisner, Environ. Sci. Technol. 38 (2004) 5165.
[57] M. Ibaraki, E.A. Sudicky, Water Resour. Res. 31 (1995) 2945.